ACS OMEGA

http://pubs.acs.org/journal/acsodf

Article

2D/2D Biochar/Bi_2WO_6 Hybrid Nanosheets with Enhanced Visible-Light-Driven Photocatalytic Activities for Organic Pollutants Degradation

Xiaolin Li, Yanan Qu, Junjie Xu, Junhui Liang, Huayu Chen, Da Chen,* and Liqun Bai*

Cite This: *ACS Omega* 2023, 8, 26882−26894

Read Online

ACCESS | Metrics & More | Article Recommendations

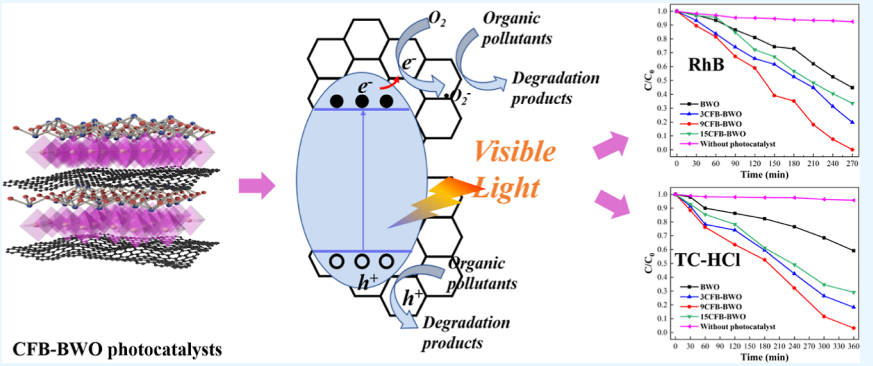

ABSTRACT: In this work, a novel two-dimensional/two-dimensional (2D/2D) hybrid photocatalyst consisting of Bi_2WO_6 (BWO) nanosheets and cotton fibers biochar (CFB) nanosheets was successfully prepared via a facile hydrothermal process. The as-prepared photocatalysts were characterized by a variety of techniques, including X-ray diffraction, scanning electron microscopy, transmission electron microscopy, X-ray photoelectron spectroscopy, and UV−vis diffuse reflectance spectroscopy. It was revealed that amorphous CFB nanosheets were uniformly immobilized on the surface of crystalline BWO nanosheets, and an intimate contact between CFB and BWO was constructed. The photocatalytic activities of the prepared BWO and CFB−BWO photocatalysts were evaluated by photocatalytic degradation of rhodamine B (RhB) and tetracycline hydrochloride (TC-HCl) in aqueous solutions under visible-light irradiation. Compared to the pristine BWO, the CFB−BWO composite photocatalysts exhibited significant enhancement in photocatalytic activities. Among all CFB−BWO samples, the 9CFB−BWO sample with the CFB mass ratio of 9% exhibited optimal photocatalytic activities for RhB or TC-HCl degradation, which was ca. 1.8 times or 2.4 times that of the pristine BWO, respectively. The improvement in photocatalytic activities of the CFB−BWO photocatalysts could be ascribed to the enhanced migration and separation of photogenerated charge carriers due to the formation of a 2D/2D interfacial heterostructure between CFB and BWO. Meanwhile, the possible mechanism of CFB−BWO for enhanced photocatalytic performance was also discussed. This work may provide a new approach to designing and developing novel BWO-based photocatalysts for the highly efficient removal of organic pollutants.

1. INTRODUCTION

Energy scarcity and environmental pollution are two of the most serious challenges confronting the world today. Hence, the concept of "Green Chemistry"[1] has been developed, which focuses on minimizing the use of non-renewable resources and eliminating pollutants from wastewater.[2−4] Photocatalysis, which directly captures and transforms unlimited solar energy into storable energy, has been regarded as one of the most efficient and ecologically beneficial techniques in "Green Chemistry". Since Fujishima and Honda's seminal photocatalytic water decomposition work in 1972,[5] photocatalytic technology has been considered as an excellent approach to eliminating water contaminants due to its moderate reaction conditions, easy operating procedure, high efficiency, and low cost.[6,7] The photocatalytic process begins with the excitation of a semiconductor photocatalyst by photons with sufficient energy. When the photocatalyst is excited, the electrons in the valence band (VB) will transition to the conduction band (CB), resulting in photogenerated electron−hole pairs.[8] These

Received: March 8, 2023
Accepted: July 12, 2023
Published: July 21, 2023

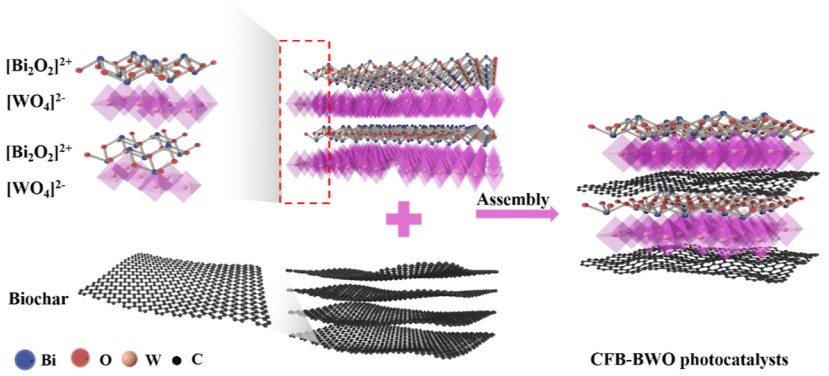

Figure 1. Schematic diagram of the CFB−BWO photocatalysts.

photogenerated electrons and holes may then migrate to the surface of the photocatalyst for a REDOX reaction, thus removing the surface-adsorbed pollutants. Therefore, the development of efficient photocatalysts is critical for broadening the practical application of the photocatalysis technology.

Bismuth tungstate (Bi_2WO_6, short for BWO), as a new kind of promising semiconductor photocatalyst, has attracted much attention due to its high structural stability, favorable photocatalytic activity, environmental friendliness, and low cost.[9] However, pure BWO nanoparticles are easy to agglomerate, which leads to a sharp decrease in the number of photocatalytic active sites and is unfavorable to the photocatalytic reaction. Comparatively, BWO nanosheets with a two-dimensional (2D) structure have a larger specific surface area, which can effectively improve the photocatalytic activity. In spite of this, due to its relatively wide band gap, poor photogenerated carrier mobility, and easy recombination of photogenerated charge carriers, the photocatalytic activity of BWO nanosheets is still poor, which greatly limits its further applications. The construction of heterojunctions is one of the methods commonly used to enhance the performance of photocatalysts. For example, Chen et al.[10] prepared a 2D/2D heterostructure of black phosphorus (BP)/BWO with oxygen vacancy for enhanced photocatalytic reduction of CO_2 to produce syngas, leading to a mild and controllable reaction process to obtain the target gas. Cao et al.[11] formed 2D/2D heterojunction Ti_3C_2/BWO hybrids by in situ growth of BWO ultrathin nanosheets on Ti_3C_2 nanosheets, which exhibited enhanced CO_2 reduction performance with their short charge-transfer distance and large contact area. Hu et al.[12] designed and fabricated a 2D/2D BP/monolayer BWO *Z*-scheme heterojunction for photocatalytic water splitting to produce H_2 with 9.15 times the performance of the original monolayer BWO.

On the other hand, 2D structured materials such as graphene and g-C_3N_4 are widely used to enhance photocatalytic performance, but the conditions for their preparation are complex and costly.[13−15] Thus, as a new type of low-cost carbon material, biochar prepared under the condition of limited oxygen has a unique 2D nanostructure, large specific surface area, excellent electrical conductivity, and abundant surface groups, which has attracted attention in the field of photocatalysis in recent years.[16,17] The introduction of biochar 2D nanosheets into semiconductor photocatalysts can greatly inhibit the aggregation of photocatalyst particles, promote the separation of photogenerated carriers, and inhibit the recombination of the photogenerated carriers, thus probably improving the photocatalytic activity.[18−23]

In recent years, the construction of 2D/2D heterostructure photocatalysts has been proven to effectively improve the photocatalytic activity.[24] This is because the 2D/2D heterostructure can greatly increase the interface contact between the two; morphological engineering can facilitate the rapid migration and separation of photogenerated carriers, thus greatly reducing the recombination rate of photogenerated carriers and thereby improving the photocatalytic activity.[11,25] In view of this, herein, cotton fiber biochar (CFB) nanosheets were used to modify the BWO nanosheets by a simple hydrothermal process, and the CFB−BWO 2D/2D heterostructure photocatalysts were thus obtained. On this basis, the photocatalytic activities of CFB−BWO were evaluated by the photodegradation of rhodamine B (RhB) and tetracycline hydrochloride (TC-HCl), and then the relationship between the added CFB mass ratio and the photocatalytic performance was explored. Meanwhile, the photocatalytic mechanism of CFB−BWO was also proposed.

2. EXPERIMENTAL SECTION

2.1. Materials. Skimmed cotton fibers were purchased from Zhejiang Agriculture and Forestry University. Bismuth nitrate pentahydrate ($Bi(NO_3)_3{\cdot}5H_2O$) and sodium tungstate dihydrate ($Na_2WO_4{\cdot}2H_2O$) were purchased from Sinopharm Chemical Reagent Co. RhB and TC-HCl were purchased from Shanghai Maclean Biochemical Co. Other chemical reagents were of analytical grade and could be used without further purification.

2.2. Preparation of CFB−BWO Composites. CFB was synthesized by the hydrothermal method. Typically, 2.000 g of cotton fibers were mixed with 60 mL of deionized water before being placed in a Teflon-lined autoclave and maintained at 170 °C for 24 h. After hydrothermal reaction, the obtained precipitates were rinsed 2−3 times with deionized water and anhydrous ethanol and then dried in a vacuum oven at 60 °C overnight. The CFB powder was thus obtained after being ground thoroughly in a mortar and pestle.

The CFB−BWO composites were also prepared by the hydrothermal method, as schematically illustrated in Figure 1. First, 1.5000 g of $Bi(NO_3)_3{\cdot}5H_2O$ was dissolved in 10 mL of 1.6 mol L^{-1} nitric acid solution. After $Bi(NO_3)_3{\cdot}5H_2O$ was completely dissolved, 10 mL of deionized water was added to dilute the solution to 20 mL to obtain the precursor solution 1. Meanwhile, 0.4728 g of $Na_2WO_4{\cdot}2H_2O$ was dissolved in 20 mL of 2.0 mol L^{-1} NaOH solution by magnetic stirring, and the precursor solution 2 was thus obtained. After that, the precursor solution 2 was added to the precursor solution 1 drop by drop

https://doi.org/10.1021/acsomega.3c01591
ACS Omega 2023, 8, 26882−26894

under magnetic stirring, and the pH value of the resulting mixed solution was adjusted to 7 by using 1.6 M HNO_3 and 2 M NaOH aqueous solutions. Subsequently, CFB was added to the above mixed solution at a certain mass percentage (relative to BWO), and a uniform dispersion was formed after magnetic stirring for 10 min and ultrasonic treatment for 30 min. The dispersion was then transferred to a 100 mL hydrothermal reactor, where it reacted at 170 °C for 24 h. After the reaction was finished, the reactor was cooled to room temperature naturally. The reaction precipitates were collected by filtering through a Brinell funnel and cleaned by deionized water several times and then dried overnight in a vacuum oven. After drying, a light brown powder of CFB−BWO composites could be obtained. The obtained products were labeled as 3CFB−BWO, 9CFB−BWO, and 15CFB−BWO according to the mass percentage (3, 9, and 15 wt %) of the added CFB relative to BWO, respectively. For comparison, BWO was also prepared using the same experimental procedure, except that CFB was not added to the precursor solution.

2.3. Characterizations. Morphological characteristics of the prepared samples were examined using a Hitachi SU8010 field-emission scanning electron microscope attached with an energy-dispersive X-ray spectrometer. Transmission electron microscopy (TEM) was recorded on a JEOL JEM 2100F microscope. The crystal phases of the prepared samples were analyzed by X-ray diffraction (XRD) using a Rigaku Ultima X-ray diffractometer with Cu as the radiation source. X-ray photoelectron spectroscopy (XPS) measurement was performed on a Thermo Scientific device using a monochromatic Al target X-ray source ($h\nu$ = 1486.6 eV) and a DLD detector. The binding energy was adjusted by carbon C 1s (284.8 eV). Fourier transform infrared (FT-IR) spectra were recorded by an infrared spectrometer (Shimadzu IR Prestige-21, Japan) to analyze the functional groups of the samples at wavelengths from 4000 to 400 cm^{-1} with a resolution better than 0.09 cm^{-1}. The nitrogen adsorption isotherms and special surface areas were obtained using an N_2 sorption analyzer (Micromeritics APSP 2460, USA). The special surface areas were calculated using the Brunauer−Emmett−Teller (BET) model, and the average pore diameters were calculated using the Barrett−Joyner−Halenda (BJH) method. Diffuse reflectance spectroscopy (DRS) was performed by a Shimadzu UV-3600i Plus UV/vis/NIR spectrophotometer using $BaSO_4$ as the reflectance standard. The electron spin resonance (ESR) result was examined by using a Bruker EMX plus-6/1 spectrometer using a spin-trap reagent (i.e., 5,5-dimethyl-L-pyrroline *N*-oxide (DMPO)) in the visible-light mode.

2.4. Photoelectrochemical Measurements. To prepare the working photoelectrode for photoelectrochemical characterization, a fluorine-doped tin oxide (FTO) conductive glass was cleaned in deionized water, soapy water, acetone, and anhydrous ethanol successively by sonication for 10 min. The working photoelectrode was prepared by doctor-blading a slurry, which was prepared by mixing the obtained photocatalyst powder and polyethylene glycol 6000 (PEG 6000) at a weight ratio of 90:10 on FTO conductive glass followed by being dried in a vacuum oven at 170 °C for 4 h. The active area of the photoelectrode was controlled to 1.0 cm × 1.0 cm, and the visible-light source was a 500 W Xe lamp assembled with a cut-off filter ($\lambda \geq 420$ nm). Photocurrent response (i−t), electrochemical impedance spectroscopy (EIS), and Mott−Schottky (M−S) curves were performed on an electrochemical workstation (CHI660C) using a standard three-electrode system with the working photoelectrode, the saturated calomel electrode (SCE) as the reference electrode, and platinum wire as the counter electrode in 0.5 mol L^{-1} Na_2SO_4 (pH = 6.8) aqueous solution.

2.5. Photocatalytic Measurements. All photocatalytic experiments were carried out in a 100 mL glass beaker containing a certain amount of the target solution and the prepared photocatalyst powder. The visible-light source was a 500 W xenon lamp with a 420 nm cut-off filter, which was placed vertically at a fixed distance of 15 cm from the glass beaker. In a typical process, 0.05 g of the prepared photocatalyst powder was dispersed in 50 mL of RhB solution (10 mg L^{-1}). Before the photocatalytic experiment started, dark adsorption was performed for 0.5 h to reach the adsorption equilibrium to exclude the effect of powder adsorption on the photocatalytic efficiency. During the photocatalysis process, about 4.0 mL of solution was taken with a pipette at predetermined time intervals, fed into a medical syringe, and filtered through a filter membrane (13 mm, 0.22 μm) to obtain a clear solution, which was subsequently transferred to a colorimetric cuvette. A UV−vis spectrometer (Shanghai Jingke 722 N UV−vis spectrometer) was used to measure the absorbance of RhB solution at the maximum spectral absorption peak (λ = 554 nm) for the evaluation of the dye degradation process. The procedure of trapping experiments was similar to the above photocatalytic experiments except that 0.1 mM of a given scavenger was added to the solution before the xenon lamp was turned on. The photogenerated holes (h^+), hydroxyl radicals ($^{\bullet}OH$), and superoxide radicals ($^{\bullet}O_2^-$) were identified using triethanolamine (TEOA), *tert*-butyl alcohol (TBA), and *p*-benzoquinone (BQ), respectively. The degradation process of TC-HCl was similar to that of RhB, except that the concentration of TC-HCl was 20 mg L^{-1} and the dosage of photocatalyst was 0.25 g L^{-1}. The absorbance values of TC-HCl at 357 nm were measured and recorded by a double-beam UV spectrophotometer (Shanghai Jingke L5S) to evaluate the degradation rate of TC-HCl. The total organic carbon (TOC) was analyzed by a multi N/C 3100 analyzer. In addition, the intermediate products of TC-HCl photocatalytic degradation were recorded and analyzed by high-performance liquid chromatography−mass spectrometry (HPLC-MS) on an Agilent 1290 HPLC-6550QTOF/MS.

2.6. Data Analysis. The Kubelka−Munk equation (eq 1) can be used to calculate the band gap energy of the prepared samples.

$$(\alpha h\nu)^n = A(h\nu - E_g) \quad (1)$$

where α is the absorption coefficient, h is the Planck's constant, ν is the frequency of light, E_g is the band gap energy, and A is a constant. For direct or indirect transition semiconductors, n is 1/2 or 2, respectively. Thus, the band gap energy (E_g) of the obtained samples can be estimated from a plot of $(\alpha h\nu)^2$ or $(\alpha h\nu)^{1/2}$ versus photon energy ($h\nu$) for direct and indirect transition, respectively.

The photocatalytic reaction was fitted by the pseudo-first-order model and the rate constant was calculated by eq 2.

$$\ln(C_0/C) = kt \quad (2)$$

where C_0 is the initial concentration of RhB solution, C is the remaining concentration of RhB solution after photodegradation at time t, k is the photocatalytic degradation rate constant, and t is the photocatalytic degradation time.

https://doi.org/10.1021/acsomega.3c01591
ACS Omega 2023, 8, 26882−26894

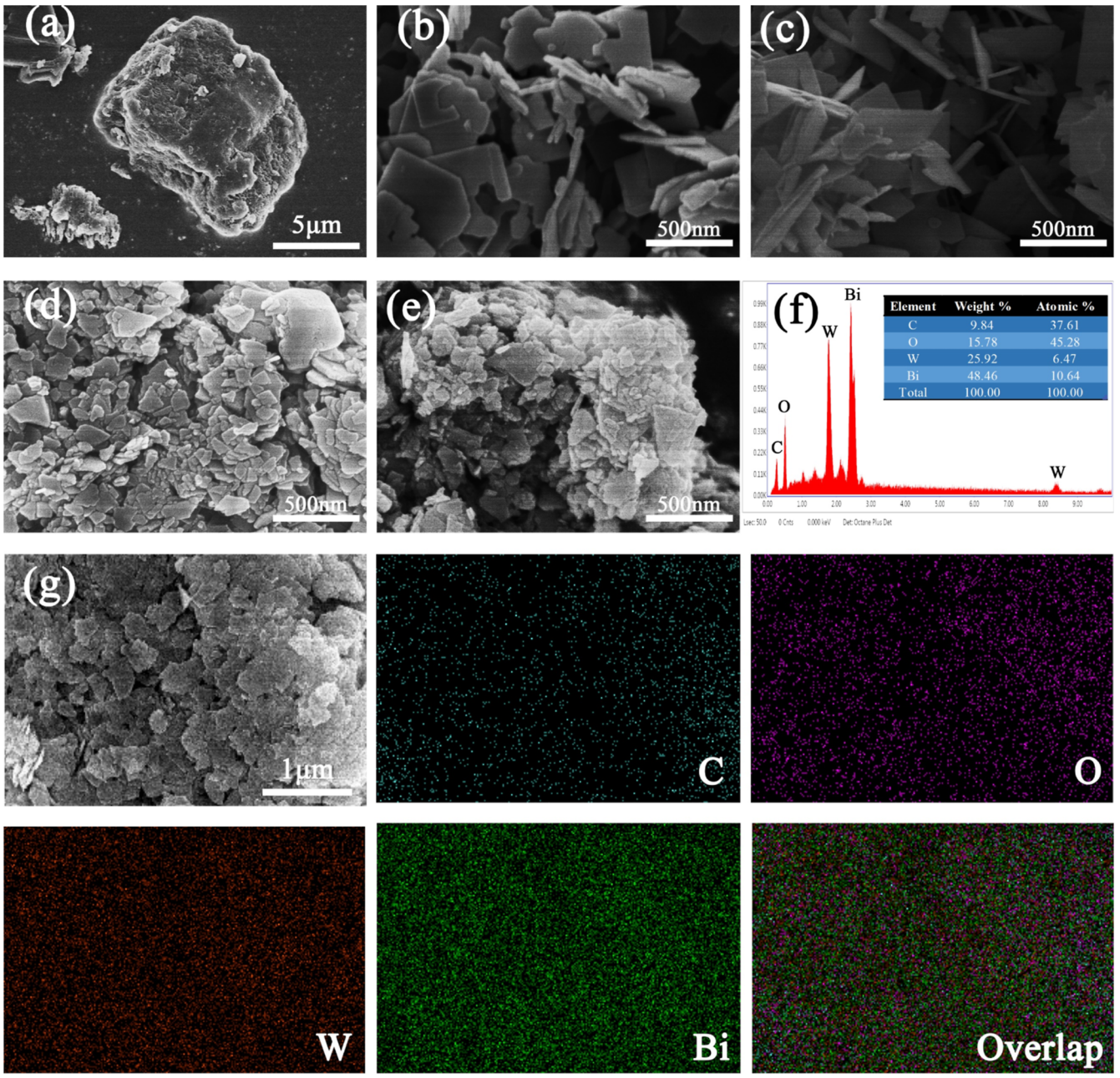

Figure 2. FESEM images of (a) CFB, (b) BWO, (c) 3CFB−BWO, (d) 9CFB−BWO, and (e) 15CFB−BWO samples; (f) SEM−EDS pattern of the 9CFB−BWO sample (the inset shows the weight and atomic percentage of each element); and (g) EDS elemental mapping of C, O, W, and Bi elements in the 9CFB−BWO sample.

The flat-band potential of the semiconductor material can be calculated by the M−S curve using the following equation (eq 3).

$$1/C^2 = 2(E - V_{fb} - k_B T/e)/A^2 e\varepsilon\varepsilon_0 N_A \quad (3)$$

where C denotes the interfacial capacitance, A denotes the electrode surface area, e denotes the electron charge, ε denotes the relative dielectric constant of the semiconductor, ε_0 denotes the vacuum dielectric constant, N_A denotes the carrier concentration, E denotes the applied potential, V_{fb} denotes the flat-band potential of the semiconductor, k_B denotes the Boltzmann constant, and T denotes the absolute temperature, respectively.

The flat-band potential obtained by eq 3 can be converted to an electrode potential with respect to the normal hydrogen electrode (NHE) using eq 4.

$$V_{NHE} = V_{SCE} + V^0_{SCE} \quad (4)$$

where V_{NHE} is the converted potential, V^0_{SCE} (0.241 V, 298 K) and V_{SCE} are the standard potential and the experimental potential measured against SCE, respectively.

3. RESULTS AND DISCUSSION

The FESEM images of the prepared CFB, BWO, and CFB−BWO composites are shown in Figure 2. It can be seen that CFB was a layered structure of nanosheets stacked together (Figure 2a), with a morphology similar to that of graphite. The structure

https://doi.org/10.1021/acsomega.3c01591
ACS Omega 2023, 8, 26882−26894

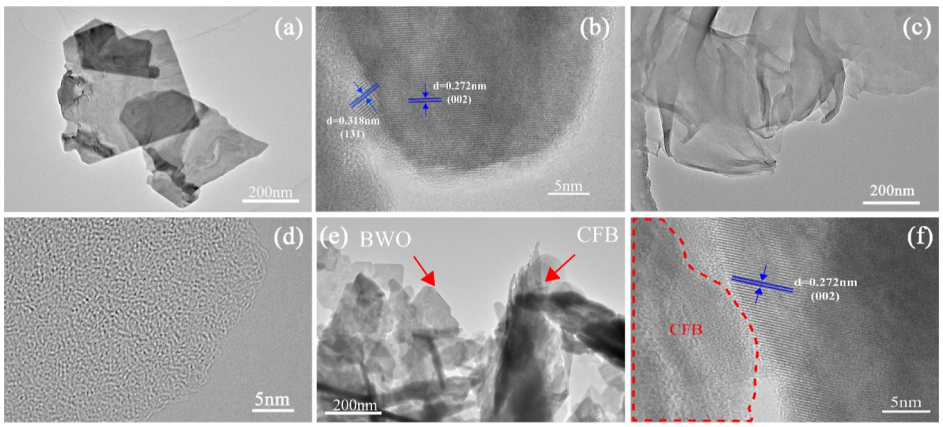

Figure 3. TEM images of (a,b) CFB, (c,d) BWO, and (e,f) 9CFB−BWO.

of BWO prepared by the hydrothermal method was also composed of nanosheets (Figure 2b), which were distinct but of different sizes. For CFB−BWO composites, the added amount of CFB had an effect on the morphology of the composites. When the added amount of CFB was only 3% of the BWO mass, 3CFB−BWO could basically maintain the 2D nanosheet structure of BWO (Figure 2c). With the increase of the amount of CFB added, the uniformity of 9CFB−BWO (Figure 2d) and 15CFB−BWO (Figure 2e) became worse, the size of the nanosheets became smaller, and more importantly, the surface of the nanosheets became rougher. Moreover, the addition of CFB, which possessed a large specific surface area, would bring a larger specific surface area to the CFB−BWO composite, which was probably favorable for the photocatalytic reaction. In addition, the close contact between CFB and BWO in the CFB−BWO composite would form a heterojunction at the interface between CFB and BWO, which could greatly promote the migration and separation of photogenerated carriers, thus improving the photocatalytic activity.[26] Furthermore, from the EDS pattern (Figure 2f) and EDS elemental mapping images (Figure 2g) of the 9CFB−BWO photocatalyst, it can be seen that the 9CFB−BWO sample contained four elements: C, O, W, and Bi, and each element was evenly distributed, indicating that the CFB and BWO were well combined together to form a heterostructured photocatalyst of CFB−BWO. Meanwhile, as seen from the inset in Figure 2f, the atomic ratio of Bi, W, and O elements in 9CFB−BWO sample was close to the stoichiometric ratio of BWO, while the mass percentage of C element was about 9.84%, which was roughly consistent with the feeding ratio.

The hydrothermally synthesized CFB presented an amorphous crumpled 2D lamellar structure (Figure 3a,b), which would facilitate the loading of massive BWO nanosheets and increase the interfacial contact between them. Figure 3c,d display the 2D nanosheets of BWO with lattice spacings of ∼0.272 and ∼0.318 nm corresponding to the (002) and (131) planes of BWO, respectively, confirming the orthorhombic crystalline structure of BWO. As shown in Figure 3e,f, the amorphous CFB nanosheets were uniformly immobilized on the surface of crystalline BWO nanosheets with intimate contact. These results provided evidence for the successful construction of CFB−BWO nanocomposites with a 2D/2D structure.

The XRD patterns of the prepared CFB, BWO, and CFB−BWO samples are shown in Figure 4. It can be seen that the CFB−BWO nanocomposites with different weight addition ratios of CFB had similar XRD patterns to that of the BWO sample. The peaks positioned at 28.2, 32.7, 47.1, 55.8, 58.6, and

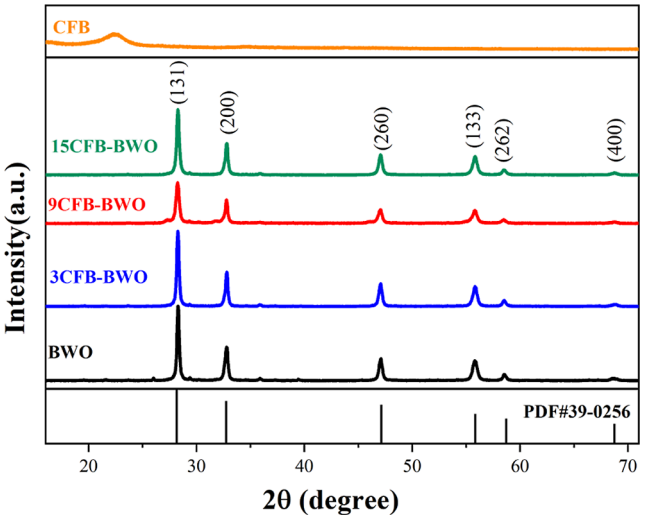

Figure 4. XRD patterns of CFB, BWO, and CFB−BWO hybrid materials with different masses of CFB.

69.0° could be indexed to (131), (200), (260), (133), (262), and (400) crystal planes of orthorhombic BWO (JCPDS no. 39-0256),[27] respectively. No typical diffraction peaks of CFB were observed in the CFB−BWO nanocomposites. This is because CFB had an amorphous structure, and its diffraction peak intensity was lower as compared with that of BWO and thus did not appear in the XRD patterns.

The surface chemical composition of the pristine CFB, BWO, and 9CFB−BWO samples was analyzed by XPS. Figure 5a shows the XPS survey spectra of the prepared CFB, BWO, and 9CFB−BWO samples, demonstrating that the CFB−BWO nanocomposites contained bismuth, tungsten, oxygen, and carbon elements deriving from CFB and BWO. For the BWO sample, the spin−orbit compositions of the Bi 4f peaks were centered at approximately 159.1 and 164.4 eV for Bi $4f_{7/2}$ and Bi $4f_{5/2}$ (Figure 5b), respectively, which could correspond to Bi^{3+} in the crystal structure. The high-resolution W 4f XPS spectra of the BWO and CFB−BWO samples are shown in Figure 5c. In the oxide form of BWO, the binding energies of W $4f_{5/2}$ and W $4f_{7/2}$ were 37.5 and 35.3 eV, respectively, which could be attributed to the existence of the W atom in the 6+ oxidation state. Compared with the pristine BWO, however, the characteristic peaks of Bi 4f and W 4f for the 9CFB−BWO sample were slightly shifted toward a lower binding energy. This indicates that the surface chemical environment of 9CFB−BWO

https://doi.org/10.1021/acsomega.3c01591
ACS Omega 2023, 8, 26882−26894

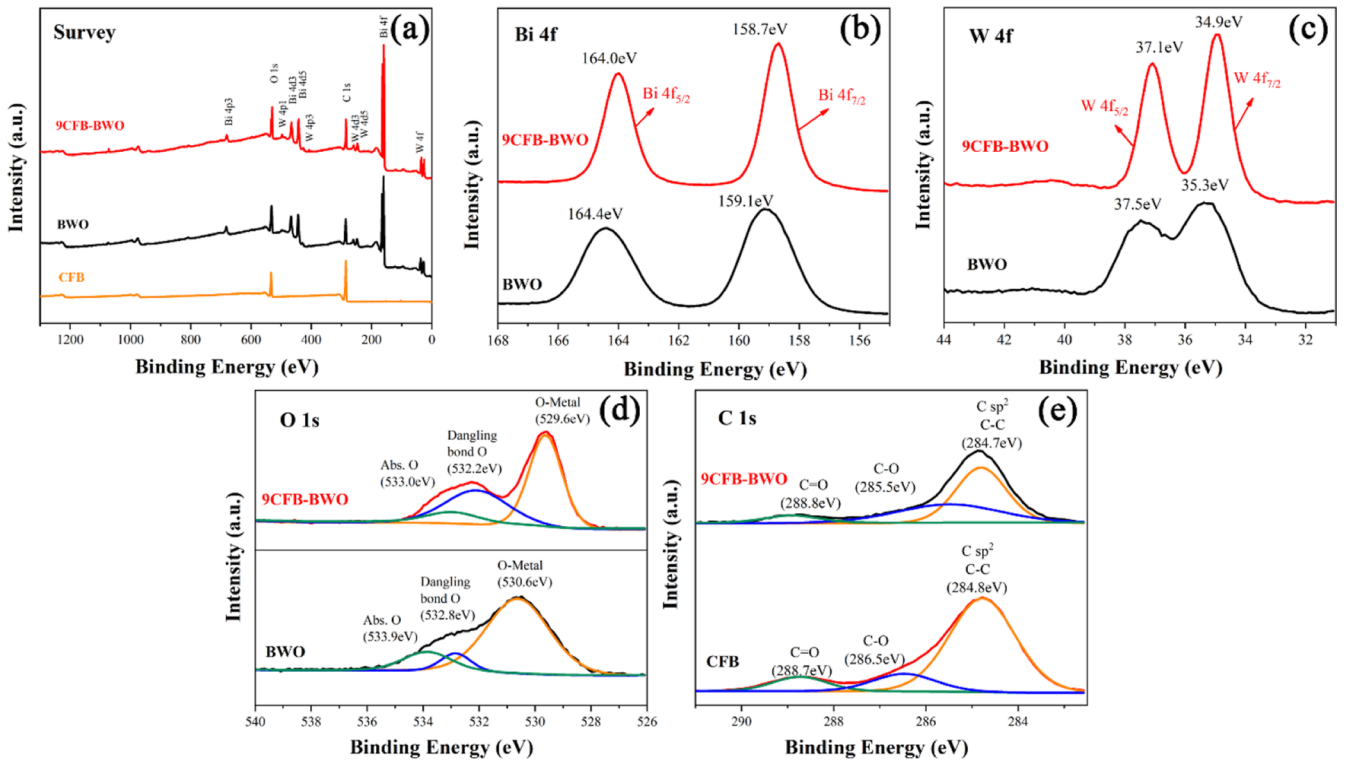

Figure 5. XPS spectra of CFB, BWO, and 9CFB−BWO. (a) Survey of the samples; (b) Bi 4f; (c) W 4f; (d) O 1s; (e) C 1s.

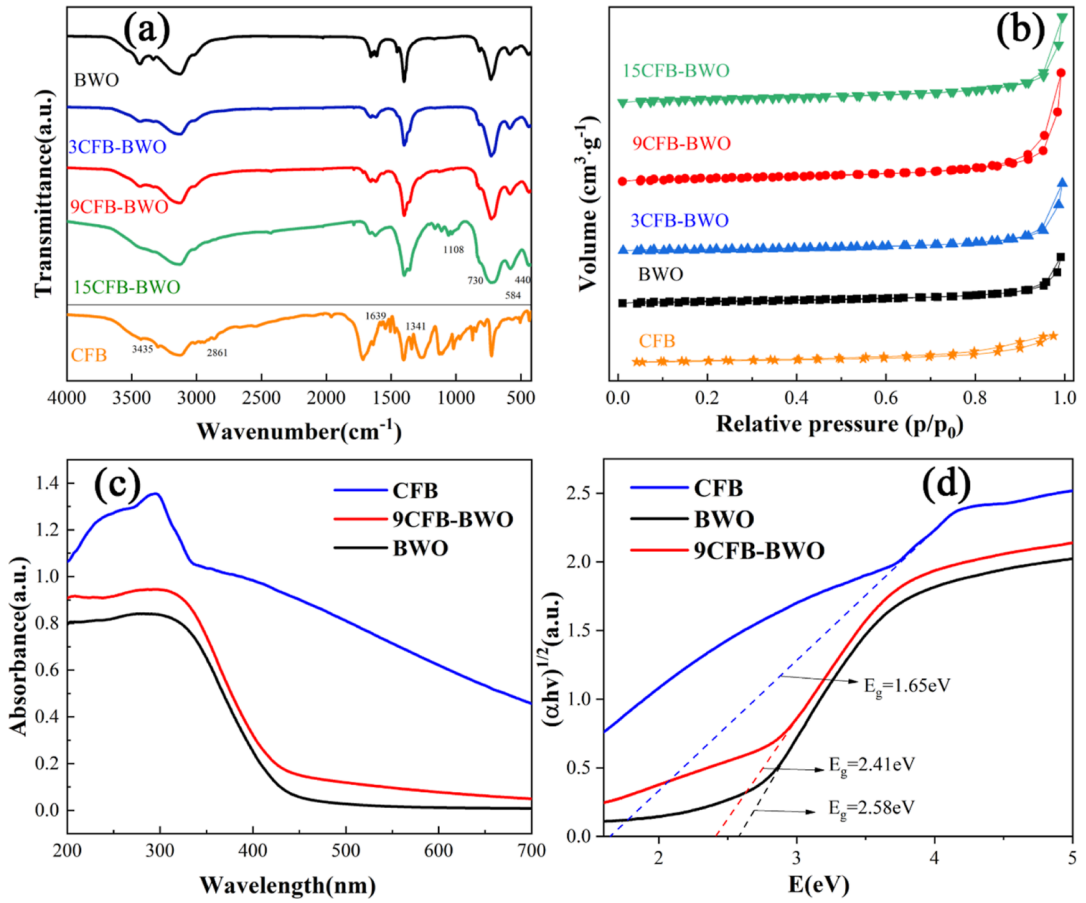

Figure 6. (a) FT-IR spectra and (b) N_2 absorption−desorption isotherms of CFB, BWO, and CFB−BWO hybrid materials with different masses of CFB; (c) UV−vis diffuse reflectance spectra and (d) band gaps of CFB, BWO, and 9CFB−BWO.

https://doi.org/10.1021/acsomega.3c01591
ACS Omega 2023, 8, 26882−26894

has changed, which could be due to the interaction between CFB and BWO in the composite. Figure 5d shows the XPS spectra of the O 1s of the BWO and 9CFB−BWO samples. It can be seen that all O 1s spectra showed three peaks. The main peak located around 530.5 eV could be associated with lattice oxygen in BWO, which was characteristic of chemical bonding between metal and oxygen atoms, while two smaller peaks positioned around 532.5 and 533.9 eV corresponded to dangling bonds and surface-adsorbed oxygen, respectively.[28,29] Figure 5e shows the C 1s high-resolution XPS spectra for the pristine CFB and 9CFB−BWO samples. The main peak at 284.7 eV could be assigned to the C−C bond with the sp^2 orbital,[18] and another two peaks centered at binding energies of 285.5 and 288.8 eV could be attributed to C−O and C═O, respectively. Furthermore, the C 1s curve of 9CFB−BWO shows that the proportion of sp^2 C−C bonding decreased obviously, while the C−O intensity increased simultaneously. This suggests that in the prepared 9CFB−BWO composites, CFB had a strong interaction with BWO through C−O−Bi bonding.[30]

The coupling of BWO with CFB can be further illustrated by the IR spectra, as shown in Figure 6a. For the pristine CFB sample, the positions of the absorption peaks were located at 2861 and 1341 cm^{-1}, corresponding to the C−H stretching vibration and the C−H in-plane bending vibration of the cellulose originating from CFB, respectively.[31,32] The absorption peaks at 3435 and 1639 cm^{-1} represented the stretching vibration of −OH and the bending vibration of −OH, respectively, indicating that the composition of CFB was rich in carbohydrates. For the prepared CFB−BWO nanocomposites, the absorption peaks at 584 and 730 cm^{-1} could be ascribed to the W−O−W bending vibration and the W−O stretching vibration of the co-angled WO_6 octahedron, respectively,[33] and the absorption peak at 440 cm^{-1} could be due to the Bi−O stretching vibration.[34] Meanwhile, the absorption peak at 1108 cm^{-1} could be attributed to the C−O−C stretching vibration induced by the combination of CFB and BWO,[35,36] and the peak intensity could increase with the increase of the added CFB amount. Moreover, the peak did not appear in the pristine BWO sample. This result confirms that the CFB and BWO nanosheets were successfully combined together in the CFB−BWO nanocomposites.

Figure 6b shows the nitrogen adsorption−desorption isotherms of the prepared CFB, BWO, and CFB−BWO samples, and the detailed values of the pore information are also listed in Table 1. It can be seen that all CFB−BWO samples show type III isotherms and H3 hysteresis loops similar to that of BWO, indicating that the addition of CFB would not change the microporous and mesoporous structures formed in the composite samples. Compared with the pristine BWO, the specific surface area, total pore volume, and average pore diameter of the CFB−BWO composite increased to some extent and showed a trend of first increasing and then decreasing with the increase of the amount of CFB added. Among all prepared samples, the 9CFB−BWO sample had the largest specific surface area, total pore diameter, and average pore diameter. The addition of appropriate CFB could greatly improve the specific surface area, total pore volume, and average pore diameter of CFB−BWO, thus significantly enhancing its adsorption capacity. Apparently, the addition of appropriate CFB could greatly improve the specific surface area, total pore volume, and average pore diameter of CFB−BWO, thus significantly enhancing its adsorption capacity. This could allow the degradation target to be adsorbed more onto the catalyst surface and increase the contact probability between the photocatalytic material and the degradation target.[37,38]

Table 1. Pore Properties of CFB and CFB−BWO Samples

sample	BET surface area ($m^2 \cdot g^{-1}$)	total pore volume ($cm^3 \cdot g^{-1}$)	average pore diameter[a] (nm)
CFB	57.9	0.17	3.8
BWO	7.2	0.03	18.0
3CFB−BWO	7.3	0.05	25.8
9CFB−BWO	11.6	0.07	25.9
15CFB−BWO	9.7	0.06	24.2

[a]Mesopore diameter calculated from the BJH method.

Figure 6c,d shows the UV−visible absorption profiles of the prepared CFB, BWO, and 9CFB−BWO composites, as well as the corresponding Tauc plots for calculating band gap energy (E_g) values.[39,40] The prepared CFB exhibited relatively strong spectral absorption capacity within the whole UV−vis range, while the prepared BWO could mainly respond to the UV−visible light with wavelengths less than 480 nm. As expected, the addition of CFB could improve the light absorption efficiency of BWO in the UV−visible region to a certain extent due to the interaction between CFB and BWO. The E_g values of the prepared BWO and 9CFB−BWO can be calculated by eq 1, where the value of n for the indirect semiconductor (BWO) is 1/2.[41] The E_g value of BWO was calculated as 2.58 eV, consistent with that reported in the literature.[42] Compared with BWO, the E_g value of the 9CFB−BWO composite was reduced to 2.41 eV, probably due to the coupling of CFB.[40]

Figure 7a shows the photodegradation RhB performance of the prepared CFB−BWO composite photocatalysts containing different CFB mass ratios in RhB aqueous solution (10 mg L^{-1}) upon visible-light irradiation. During the degradation process, the concentration of the catalyst was 1 g L^{-1}. For the pristine BWO, the degradation rate of RhB was 55.2% after 270 min of visible-light irradiation. Comparatively, the photocatalytic activities of all prepared CFB−BWO composites increased to a large extent. Moreover, with the increase of the mass ratio of CFB, the photocatalytic degradation efficiency of RhB by the CFB−BWO composites first increased and then decreased, reaching a maximum degradation rate (99.9%) at a mass ratio of 9%. When extra CFB nanosheets were immobilized on the surface of BWO nanosheets, the intrinsic light absorption of BWO could be inhibited, resulting in poorer photogenerated charge production efficiency, as demonstrated by the photocurrent response spectra below. Figure 7b shows the proposed pseudo-first-order kinetic model based on visible-light degradation in accordance with eq 2.[43] It is obvious that 9CFB−BWO had the highest value of photocatalytic degradation rate constant (k) value among all prepared samples, indicating the fastest dye degradation process.[44] In addition, the photocatalytic degradation efficiency of 9CFB−BWO remained almost unchanged after five cycles (Figure 7c), demonstrating the excellent photocatalytic stability of the composite. Similarly, 9CFB−BWO showed much higher photocatalytic activities (degradation rate: 96.8%) than the pristine BWO (degradation rate: 40.9%) for the degradation of TC-HCl in 360 min under visible-light irradiation, as shown in Figure 7d, proving the feasibility and practicability of using the CFB−BWO composites to remove organic pollutants from wastewater.[45−47] Figure 7e

https://doi.org/10.1021/acsomega.3c01591
ACS Omega 2023, 8, 26882−26894

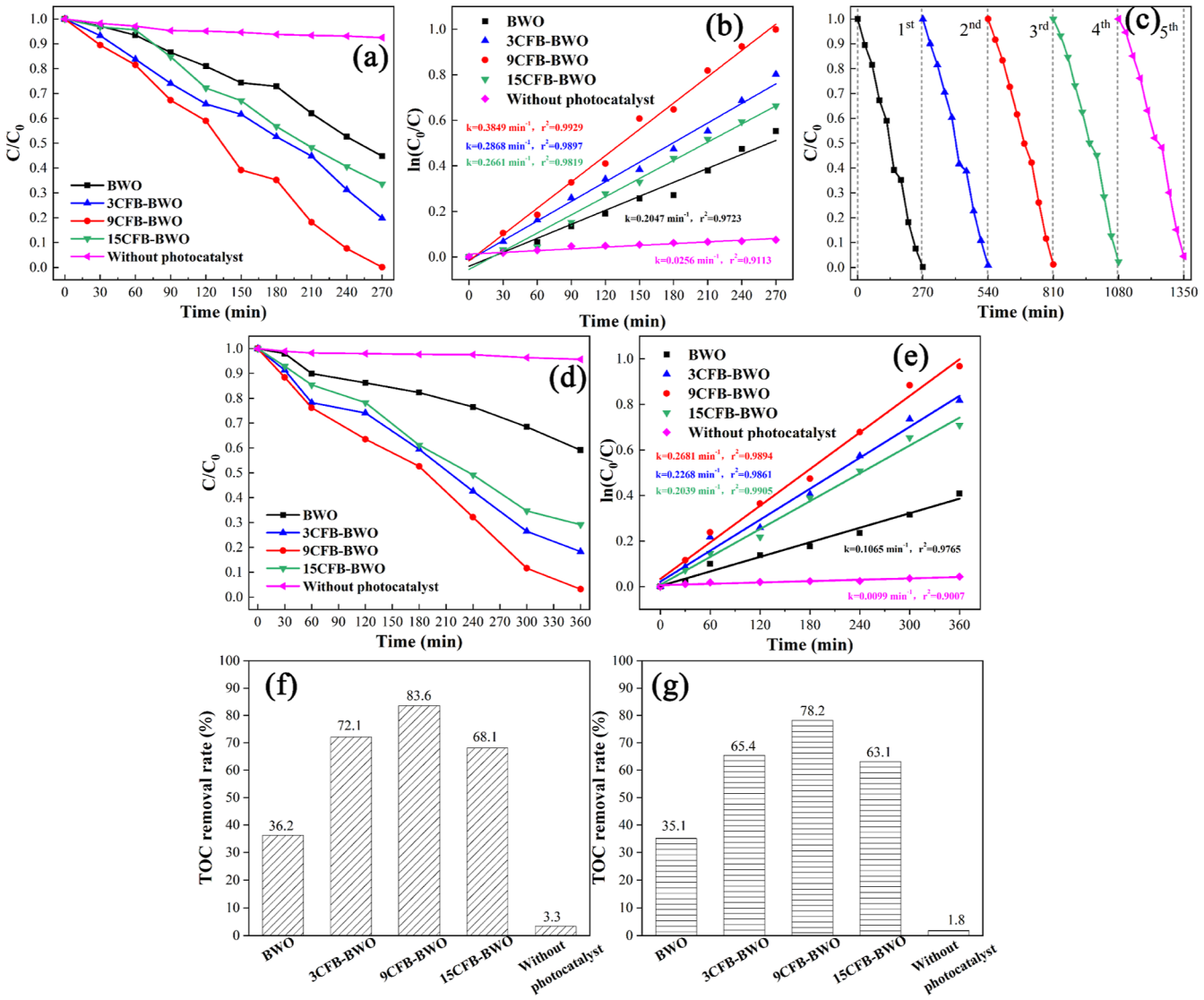

Figure 7. (a,b) Removal efficiency and pseudo-first-order kinetic fitting of the degradation of RhB; (c) cycling runs for the photodegradation of RhB in the presence of 9CFB−BWO under visible-light irradiation; (d,e) removal efficiency and pseudo-first-order kinetic fitting of the degradation of TC-HCl; and (f,g) TOC removal rate of RhB and TC-HCl.

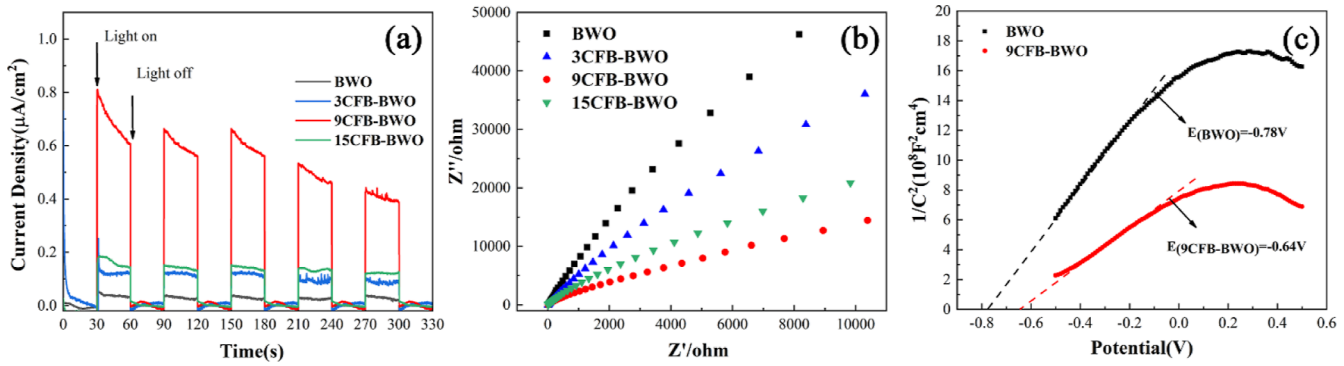

Figure 8. (a) Transient photocurrent response; (b) EIS for CFB−BWO hybrid materials with different masses of CFB; and (c) M−S curves of BWO and 9CFB−BWO.

displays the proposed pseudo-first-order kinetic model identical to the results of photodegradation experiments.

TOC analysis was performed afterward to further determine the mineralization degree of the organic pollutants and the TOC removal rates of RhB and TC-HCl from various samples. As shown in Figure 7f, the TOC removal rate was only 36.2% when RhB was degraded by pure BWO. Meanwhile, about 72.1, 83.6, and 68.1% of the TOC were removed when RhB was photodegraded by 3CFB−BWO, 9CFB−BWO, and 15CFB−BWO samples, respectively; and the TOC removal rate of RhB was

https://doi.org/10.1021/acsomega.3c01591
ACS Omega 2023, 8, 26882−26894

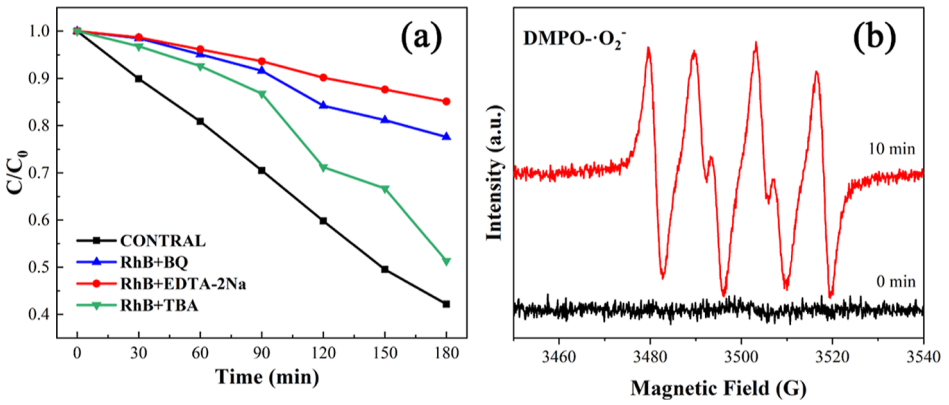

Figure 9. (a) Trapping experiment of active species during the photocatalytic degradation of RhB and (b) ESR spectra of DMPO−O_2^- for 9CFB−BWO under visible-light irradiation.

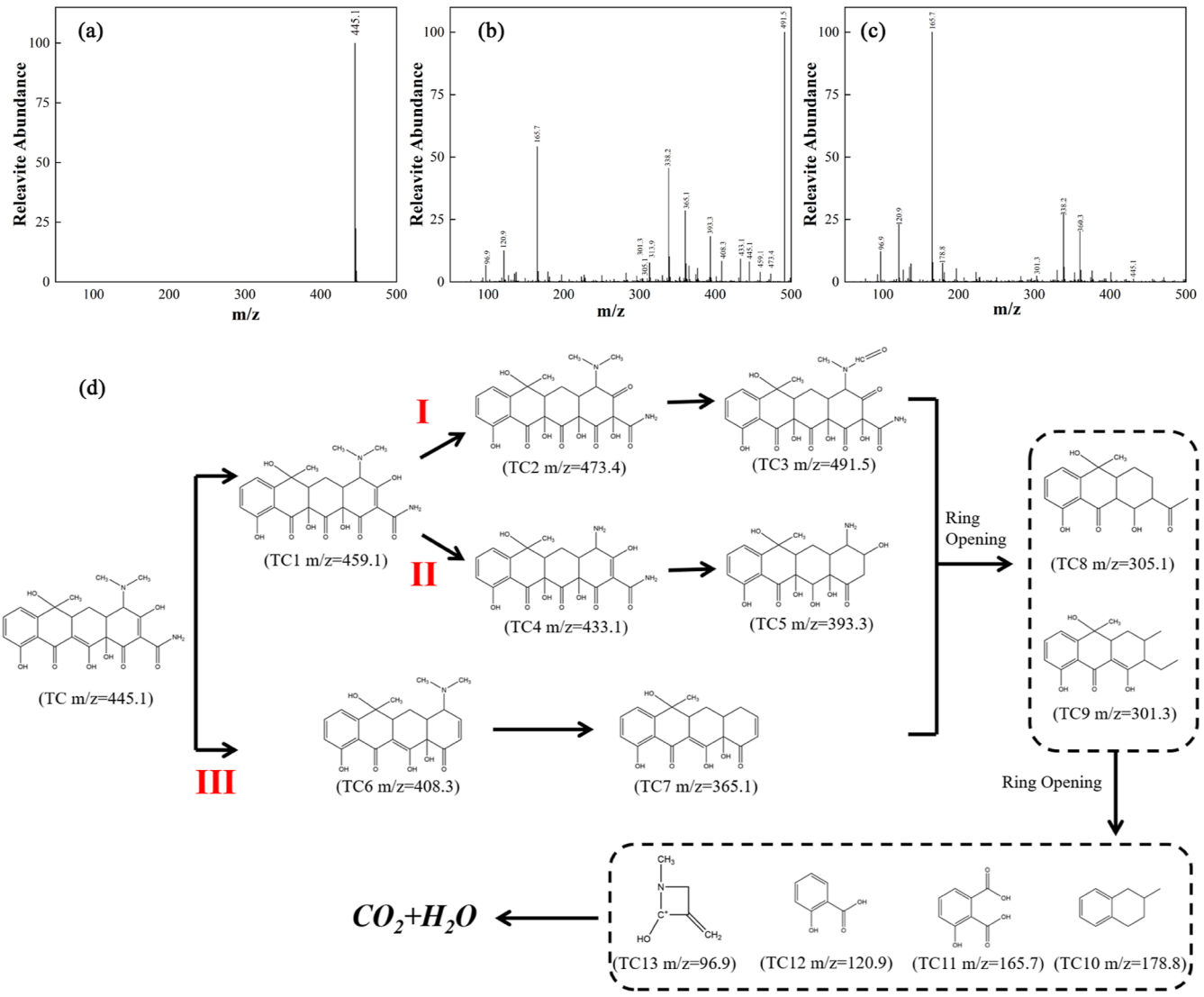

Figure 10. *m*/*z* of degrading TC-HCl over 9CFB−BWO: (a) initial solution, (b) degradation in 3 h, (c) degradation in 6 h; and (d) proposed degradation pathways of TC-HCl.

only 3.3% under visible-light irradiation without the catalyst. Similarly, as can be seen from Figure 7g, when pure BWO, 3CFB−BWO, 9CFB−BWO, and 15CFB−BWO were used for photocatalytic degradation of TC-HCl, the TOC removal rates were 35.1, 65.4, 78.2, and 63.1%, respectively, and the TOC removal rate of TC-HCl was only 1.8% under visible-light irradiation without the catalyst. Apparently, compared with BWO, the CFB−BWO composites were able to mineralize more organic pollutant molecules and convert them into inorganic byproducts like CO_2 and H_2O. The TOC removal rate results

https://doi.org/10.1021/acsomega.3c01591
ACS Omega 2023, 8, 26882−26894

further reveal that the introduction of CFB could significantly enhance the photodegradation capability of the BWO for organic pollutants mineralization in wastewater.

Figure 8 shows the photocurrent response (i–t), EIS, and M–S curves of the prepared samples. As seen in Figure 8a, all CFB–BWO samples displayed much higher photocurrent intensities than the pristine BWO upon visible-light irradiation at a set time interval, with 9CFB–BWO exhibiting the highest photocurrent intensity. Higher photocurrent values, it is usually assumed, mean that more electron–hole pairs may be effectively created and separated.[48] The presence of CFB in the composites could provide higher carrier migration efficiency and better carrier stabilization,[14] thus resulting in higher photocurrent intensity. Moreover, the coupling of CFB and BWO could be expected to establish an electronic pathway between the two to promote the interfacial charge separation efficiency.[49] In general, the interfacial charge separation efficiency can be investigated by the EIS data, in which the radius of the arc can reflect the characteristic of the interfacial charge-transfer process at the corresponding electrode/electrolyte interface. That is, the smaller the radius, the lower the corresponding charge-transfer resistance.[50,51] As shown in Figure 8b, the arc radius of 9CFB–BWO was substantially smaller than that of BWO, indicating that 9CFB–BWO exhibited a lower charge-transfer resistance. This also suggests that the addition of a certain amount of CFB could enhance the charge-transfer efficiency at the complicated interface between BWO and CFB, thus inhibiting the recombination of electron–hole pairs. To further elucidate the putative mechanism for the enhanced photocatalytic activity of the CFB–BWO composite, the flat-band potentials of BWO and 9CFB–BWO were estimated by analyzing M-S plots according to eq 3. From the M–S plots (Figure 8c), it can be observed that both the pristine BWO and 9CFB–BWO composite had positive slopes, indicating that the two samples were n-type semiconductors.[52] By extrapolating to $1/C^2 = 0$, the positions of the flat-band potentials (V_{fb}) of BWO and 9CFB–BWO were determined by the intersection points to be −0.776 and −0.676 eV (vs SCE), respectively, which could be further converted to −0.535 and −0.435 eV (vs NHE) using eq 4.[53,54]

In order to figure out the active species during the photocatalytic process, the photocatalytic performances of 9CFB–BWO for the degradation of RhB in the presence of various scavengers were investigated, and the results are shown in Figure 9a. When different scavengers were added, the photocatalytic degradation of RhB by the 9CFB–BWO composite was inhibited to varying degrees. The addition of TEOA (a hole (h^+) scavenger) or BQ (a superoxide radical ($^\bullet O_2^-$) scavenger) could significantly reduce the photocatalytic degradation efficiency of 9CFB–BWO. In contrast, the addition of TBA (a hydroxyl radicals ($^\bullet OH$) scavenger) had a minor inhibitory influence on the photocatalytic efficiency of 9CFB–BWO. The above trapping experiments clearly reveal that the predominant active species for photodegradation of organic pollutants by the 9CFB–BWO composite were photogenerated holes (h^+)[55] and superoxide radicals ($^\bullet O_2^-$)[56,57] rather than hydroxyl radicals ($^\bullet OH$).[58] Meanwhile, the in situ ESR spin-trap experiment with DMPO was also carried out under visible-light irradiation to further clarify the active species involved in the photocatalytic degradation of RhB by the prepared 9CFB–BWO composite photocatalyst. As seen in Figure 9b, no ESR signals were detected before light irradiation, and strong ESR signals were observed after light irradiation for 10 min, which could be ascribed to the presence of DMPO–$^\bullet O_2^-$,[59] further confirming the formation of superoxide radicals ($^\bullet O_2^-$) during the photocatalytic degradation of RhB by 9CFB–BWO.

The HPLC–MS measurements were performed to identify the reaction process of TC-HCl photocatalytic degradation, and the results are shown in Figure 10a–c. The TC molecules could be identified by the peak at m/z = 445.1. After 3 h (Figure 10b) and 6 h (Figure 10c) irradiation with visible light, this peak almost disappeared, while the other fragments gradually increased, demonstrating that TC molecules had been broken down into smaller molecules. On this basis, possible intermediates of TC-HCl degradation could be determined and are schematically illustrated in Figure 10d.

As known, *N*-methyl, amino group, ketone group, and carbon–carbon double bonds are reactive sites susceptible to attack by free radicals during photocatalysis, and the reactivity between carbon–carbon double bonds and free radicals is the strongest.[60,61] In our case, the degradation pathway of TC consisted of two main parts: the removal of specific functional groups and ring-opening reactions. The process of functional group removal could be divided into three main pathways. The first path is that the double bonds of TC (m/z = 445.1) could undergo a cycloaddition reaction and gradually rearrange into TC1 (m/z = 459.1), TC2 (m/z = 473.4), and TC3 (m/z = 491.5) under continuous attack of active free radicals. In the second path, TC1 could be demethylated by h^+ or other active free radicals to produce TC4 (m/z = 433.1), and the subsequent addition of electrons to the ketone position of TC4 could lead to the deamidation process, resulting in TC5 (m/z = 393.3). In the third path, raw TC could form TC6 (m/z = 408.3) by the removal of $-CONH_2$ and $-OH$ groups. TC6 could subsequently lose the $-N(CH_3)_2$ group to produce TC7 (m/z = 365.1). Intermediates for the ring-opening process could include TC8 (m/z = 305.1) and TC9 (m/z = 301.3). The degradation products [i.e., TC10 (m/z = 178.8), TC11 (m/z = 165.7), TC12 (m/z = 120.9), and TC13 (m/z = 96.9)] could be eventually mineralized to CO_2, H_2O, and NH_4^+ under the action of active free radicals such as h^+ and $^\bullet O_2^-$.

Generally speaking, the CB potential (E_{CB}) of an n-type semiconductor is close to the value of V_{fb}. Thus, the E_{CB} values of the prepared BWO and 9CFB–BWO were ca. −0.54 and −0.44 eV (vs NHE), respectively.[53] Combined with the band gap energy (E_g) values from the above DRS results, the VB potentials (E_{VB}) of BWO and 9CFB–BWO could be determined as 1.80 and 1.97 eV (vs NHE), respectively. Since the $^\bullet OH/OH^-$ redox potential (1.99 eV vs NHE) is more positive than the E_{VB} value of 9CFB–BWO (1.97 eV vs NHE), this would not allow OH^- to react with photogenerated holes (h^+) to form hydroxyl radicals ($^\bullet OH$). Therefore, $^\bullet OH$ had less influence on the photocatalytic activity.[62] In contrast, the E_{CB} value of 9CFB–BWO (−0.44 eV vs NHE) was more negative than the $O_2/^\bullet O_2^-$ redox potential (−0.33 eV vs NHE), thus allowing photogenerated electrons to react with O_2 to form $^\bullet O_2^-$ radicals. Apparently, the photogenerated holes and superoxide radicals would constitute the main active species for the photocatalytic degradation of RhB by 9CFB–BWO, as also confirmed by the above trapping experiments and ESR results.

Based on the above results and discussion, the possible mechanism of the CFB–BWO for enhanced photocatalytic degradation performance was also proposed, as schematically illustrated in Scheme 1. When the CFB–BWO composite was irradiated by UV–visible light with photon energy larger than its band gap energy, BWO would rapidly generate electron–hole pairs. The photogenerated electrons could then immediately

https://doi.org/10.1021/acsomega.3c01591
ACS Omega 2023, 8, 26882–26894

Scheme 1. Schematic Illustration of the Photocatalytic Removal of RhB and TC-HCl by 9CFB−BWO Under Visible-Light Irradiation

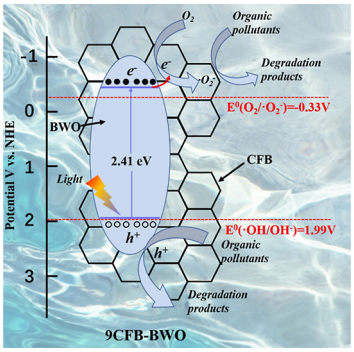

transfer to the CB of BWO. In view of the excellent electronic conductivity of the biochar of CFB,[63] the photogenerated electrons in the CB of BWO could be effectively transferred to the surface of CFB nanosheets, which could promote the effective separation of photogenerated charge carriers and thus inhibit the recombination of photogenerated charge carriers to a large extent.[64] During the photocatalytic degradation process, the photogenerated electrons transferred to the surface of CFB would react with the adsorbed oxygen on the surface to form superoxide free radicals. Consequently, superoxide free radicals formed on the surface of CFB and photogenerated holes in the VB of BWO would decompose organic pollutants (e.g., RhB, TC-HCl) adsorbed on the surface to turn into non-toxic and harmless small molecules through their strong oxidation, respectively. According to the above discussions, the possible photocatalytic reactions could be expressed as follows

$$Bi_2WO_6 + h\nu \rightarrow h^+(Bi_2WO_6) + e^-(Bi_2WO_6) \quad (5)$$

$$e^-(Bi_2WO_6) \rightarrow e^-(\text{biochar}) \quad (6)$$

$$O_2(\text{biochar}) + e^-(\text{biochar}) \rightarrow {}^{\bullet}O_2^-(\text{biochar}) \quad (7)$$

$${}^{\bullet}O_2^-(\text{biochar}) + \text{organic pollutants} \rightarrow \text{degraded products} \quad (8)$$

$$h^+(Bi_2WO_6) + \text{organic pollutants} \rightarrow \text{degraded products} \quad (9)$$

4. CONCLUSIONS

In summary, a novel CFB−BWO 2D/2D photocatalyst was successfully constructed via a hydrothermal process, in which cotton fibers were used as the source of biochar. It was revealed that amorphous CFB nanosheets were uniformly immobilized on the surface of crystalline BWO nanosheets with an intimate contact. Compared with the pristine BWO, the prepared CFB−BWO composites exhibited much higher photocatalytic activities for RhB degradation. With increasing the mass ratio of CFB from 3 to 15%, the photocatalytic activity for RhB degradation upon visible-light irradiation first increased and then decreased. When the mass ratio of CFB was 9%, the optimal photocatalytic degradation efficiency was achieved, which was much higher than that of the pristine BWO. The enhanced photocatalytic performance was mainly attributed to the formation of a 2D/2D interfacial heterostructure between CFB and BWO. The coupling of CFB nanosheets could provide a reliable and fast transfer path for the migration and separation of photogenerated carriers in the composite, thus effectively inhibiting the recombination of photogenerated carriers. Moreover, the presence of CFB nanosheets could also improve the specific surface area of the composite to offer more active sites for the photocatalytic degradation of target organic pollutants. Thus, this work may provide a new approach to designing and developing novel BWO-based photocatalysts for the highly efficient removal of organic pollutants.

AUTHOR INFORMATION

Corresponding Authors

Da Chen − *College of Materials and Chemistry, China Jiliang University, Hangzhou, Zhejiang 310018, China;* orcid.org/0000-0001-7854-7135; Email: dchen_80@hotmail.com

Liqun Bai − *College of Chemistry and Materials Engineering, Zhejiang Agriculture and Forestry University, Hangzhou, Zhejiang Province 311300, China*; Email: bailiqun78@163.com

Authors

Xiaolin Li − *College of Chemistry and Materials Engineering, Zhejiang Agriculture and Forestry University, Hangzhou, Zhejiang Province 311300, China*

Yanan Qu − *College of Chemistry and Materials Engineering, Zhejiang Agriculture and Forestry University, Hangzhou, Zhejiang Province 311300, China*

Junjie Xu − *College of Chemistry and Materials Engineering, Zhejiang Agriculture and Forestry University, Hangzhou, Zhejiang Province 311300, China*

Junhui Liang − *College of Materials and Chemistry, China Jiliang University, Hangzhou, Zhejiang 310018, China;* orcid.org/0000-0002-0508-8297

Huayu Chen − *College of Materials and Chemistry, China Jiliang University, Hangzhou, Zhejiang 310018, China;* orcid.org/0000-0002-9396-0793

Complete contact information is available at: https://pubs.acs.org/10.1021/acsomega.3c01591

Notes

The authors declare no competing financial interest.

ACKNOWLEDGMENTS

This work was financially supported by the National Natural Science Foundation of China (no. 51972294), the Natural Science Foundation of Zhejiang Province (no. LQ20F040007), and the Fundamental Research Funds for the Provincial Universities of Zhejiang (nos. 2022YW62, 2021YW35).

REFERENCES

(1) Li, D.; Shi, W. Recent developments in visible-light photocatalytic degradation of antibiotics. *Chin. J. Catal.* **2016**, *37*, 792−799.

(2) Chen, S.; Huang, D.; Cheng, M.; Lei, L.; Chen, Y.; Zhou, C.; Deng, R.; Li, B. Surface and interface engineering of two-dimensional bismuth-based photocatalysts for ambient molecule activation. *J. Mater. Chem. A* **2021**, *9*, 196−233.

(3) Tan, X. F.; Liu, Y. G.; Gu, Y. L.; Xu, Y.; Zeng, G. m.; Hu, X. j.; Liu, S. b.; Wang, X.; Liu, S. m.; Li, J. Biochar-based nano-composites for the decontamination of wastewater: A review. *Bioresour. Technol.* **2016**, *212*, 318−333.

(4) Sabri, M.; Habibi-Yangjeh, A.; Rahim Pouran, S.; Wang, C. Titania-activated persulfate for environmental remediation: the state of the art. *Catal. Rev.* **2023**, *65*, 118−173.

https://doi.org/10.1021/acsomega.3c01591
ACS Omega 2023, 8, 26882−26894

(5) Fujishima, A.; Honda, K. Electrochemical Photolysis of Water at a Semiconductor Electrode. *Nature* **1972**, *238*, 37−38.
(6) Chen, M. J.; Yao, J.; Huang, Y.; Gong, H.; Chu, W. Enhanced photocatalytic degradation of ciprofloxacin over Bi_2O_3/$(BiO)_2CO_3$ heterojunctions: Efficiency, kinetics, pathways, mechanisms and toxicity evaluation. *Chem. Eng. J.* **2018**, *334*, 453−461.
(7) Miao, D. G.; Jiang, S. X.; Liu, J.; Ning, X.; Shang, S. M.; Xu, J. T. Fabrication of copper and titanium coated textiles for sunlight management. *J. Mater. Sci.: Mater. Electron.* **2017**, *28*, 9852−9858.
(8) Donar, Y. O.; Bilge, S.; Sinag, A.; Pliekhov, O. TiO_2/Carbon Materials Derived from Hydrothermal Carbonization of Waste Biomass: A Highly Efficient, Low-Cost Visible-Light-Driven Photocatalyst. *ChemCatchem* **2018**, *10*, 1134−1139.
(9) Chen, T.; Liu, L. Z.; Hu, C.; Huang, H. W. Recent advances on Bi_2WO_6-based photocatalysts for environmental and energy applications. *Chin. J. Catal.* **2021**, *42*, 1413−1438.
(10) Chen, C.; Hu, J. D.; Yang, X. G.; Yang, T. Y.; Qu, J. F.; Guo, C. X.; Li, C. M. Ambient-Stable Black Phosphorus-Based 2D/2D S-Scheme Heterojunction for Efficient Photocatalytic CO_2 Reduction to Syngas. *ACS Appl. Mater. Interfaces* **2021**, *13*, 20162−20173.
(11) Cao, S. W.; Shen, B. J.; Tong, T.; Fu, J. W.; Yu, J. G. 2D/2D Heterojunction of Ultrathin MXene/Bi_2WO_6 Nanosheets for Improved Photocatalytic CO_2 Reduction. *Adv. Funct. Mater.* **2018**, *28*, 1800136.
(12) Hu, J. D.; Chen, D. Y.; Mo, Z.; Li, N. J.; Xu, Q. F.; Li, H.; He, J. H.; Xu, H.; Lu, J. M. Z-Scheme 2D/2D Heterojunction of Black Phosphorus/Monolayer Bi_2WO_6 Nanosheets with Enhanced Photocatalytic Activities. *Angew. Chem., Int. Ed.* **2019**, *58*, 2073−2077.
(13) Ahmed, M. A.; Mohamed, A. A. Recent progress in semiconductor/graphene photocatalysts: synthesis, photocatalytic applications, and challenges. *RSC Adv.* **2023**, *13*, 421−439.
(14) Akhundi, A.; Badiei, A.; Ziarani, G. M.; Habibi-Yangjeh, A.; Munoz-Batista, M. J.; Luque, R. Graphitic carbon nitride-based photocatalysts: Toward efficient organic transformation for value-added chemicals production. *Mol. Catal.* **2020**, *488*, 110902.
(15) Akhundi, A.; Habibi-Yangjeh, A.; Abitorabi, M.; Rahim Pouran, S. Review on photocatalytic conversion of carbon dioxide to value-added compounds and renewable fuels by graphitic carbon nitride-based photocatalysts. *Catal. Rev.* **2019**, *61*, 595−628.
(16) Mian, M. M.; Liu, G. J. Recent progress in biochar-supported photocatalysts: synthesis, role of biochar, and applications. *RSC Adv.* **2018**, *8*, 14237−14248.
(17) Fito, J.; Kefeni, K. K.; Nkambule, T. T. I. The potential of biochar-photocatalytic nanocomposites for removal of organic micropollutants from wastewater. *Sci. Total Environ.* **2022**, *829*, 154648.
(18) Geng, A. B.; Xu, L. J.; Gan, L.; Mei, C. T.; Wang, L. J.; Fang, X. Y.; Li, M. R.; Pan, M. Z.; Han, S. G.; Cui, J. Q. Using wood flour waste to produce biochar as the support to enhance the visible-light photocatalytic performance of BiOBr for organic and inorganic contaminants removal. *Chemosphere* **2020**, *250*, 126291.
(19) Zuo, X. J.; Chen, M. D.; Fu, D. F.; Li, H. The formation of alpha-FeOOH onto hydrothermal biochar through H_2O_2 and its photocatalytic disinfection. *Chem. Eng. J.* **2016**, *294*, 202−209.
(20) Pi, L.; Jiang, R.; Zhou, W. C.; Zhu, H.; Xiao, W.; Wang, D. H.; Mao, X. H. g-C_3N_4 Modified biochar as an adsorptive and photocatalytic material for decontamination of aqueous organic pollutants. *Appl. Surf. Sci.* **2015**, *358*, 231−239.
(21) Zhang, H. Y.; Wang, Z. W.; Li, R. N.; Guo, J. L.; Li, Y.; Zhu, J. M.; Xie, X. Y. TiO_2 supported on reed straw biochar as an adsorptive and photocatalytic composite for the efficient degradation of sulfamethoxazole in aqueous matrices. *Chemosphere* **2017**, *185*, 351−360.
(22) Yan, Y.; Tang, X.; Ma, C. C.; Huang, H.; Yu, K. S.; Liu, Y.; Lu, Z. Y.; Li, C. X.; Zhu, Z.; Huo, P. W. A 2D mesoporous photocatalyst constructed by the modification of biochar on BiOCl ultrathin nanosheets for enhancing the TC-HCl degradation activity. *New J. Chem.* **2020**, *44*, 79−86.
(23) Cao, T. T.; Cui, H.; Zhang, Q. W.; Cui, C. W. Facile synthesis of Co(II)-BiOCl@biochar nanosheets for photocatalytic degradation of p-nitrophenol under vacuum ultraviolet (VUV) irradiation. *Appl. Surf. Sci.* **2021**, *559*, 149938.
(24) Yu, H. J.; Dai, M.; Zhang, J.; Chen, W. H.; Jin, Q.; Wang, S. G.; He, Z. L. Interface Engineering in 2D/2D Heterogeneous Photocatalysts. *Small* **2022**, *19*, 2205767.
(25) Akhundi, A.; Zaker Moshfegh, A.; Habibi-yangjeh, A.; Sillanpää, M. Simultaneous Dual-Functional Photocatalysis by g-C_3N_4-Based Nanostructures. *ACS ES&T Engg* **2022**, *2*, 564−585.
(26) Chen, S. H.; Yin, Z.; Luo, S. L.; Li, X. J.; Yang, L. X.; Deng, F. Photoreactive mesoporous carbon/Bi_2WO_6 composites: Synthesis and reactivity. *Appl. Surf. Sci.* **2012**, *259*, 7−12.
(27) Tian, J.; Sang, Y. H.; Yu, G. W.; Jiang, H. D.; Mu, X. N.; Liu, H. A Bi_2WO_6-Based Hybrid Photocatalyst with Broad Spectrum Photocatalytic Properties under UV, Visible, and Near-Infrared Irradiation. *Adv. Mater.* **2013**, *25*, 5075−5080.
(28) Lei, F. C.; Sun, Y. F.; Liu, K. T.; Gao, S.; Liang, L.; Pan, B. C.; Xie, Y. Oxygen Vacancies Confined in Ultrathin Indium Oxide Porous Sheets for Promoted Visible-Light Water Splitting. *J. Am. Chem. Soc.* **2014**, *136*, 6826−6829.
(29) Zhang, N.; Chen, D.; Niu, F.; Wang, S.; Qin, L. S.; Huang, Y. X. Enhanced visible light photocatalytic activity of Gd-doped $BiFeO_3$ nanoparticles and mechanism insight. *Sci. Rep.* **2016**, *6*, 26467.
(30) Chen, M. X.; Dai, Y. Z.; Guo, J.; Yang, H. T.; Liu, D. N.; Zhai, Y. L. Solvothermal synthesis of biochar@$ZnFe_2O_4$/BiOBr Z-scheme heterojunction for efficient photocatalytic ciprofloxacin degradation under visible light. *Appl. Surf. Sci.* **2019**, *493*, 1361−1367.
(31) Li, Y.; Liu, J.; Huang, X.; Yu, J. Carbon-modified Bi_2WO_6 nanostructures with improved photocatalytic activity under visible light. *Dalton Trans.* **2010**, *39*, 3420−3425.
(32) Zhang, G.; Lü, F.; Li, M.; Yang, J.; Zhang, X.; Huang, B. Synthesis of nanometer Bi_2WO_6 synthesized by sol-gel method and its visible-light photocatalytic activity for degradation of 4BS. *J. Phys. Chem. Solids* **2010**, *71*, 579−582.
(33) Zhu, J.; Wang, J. G.; Bian, Z. F.; Cao, F. G.; Li, H. X. Solvothermal synthesis of highly active Bi_2WO_6 visible photocatalyst. *Res. Chem. Intermed.* **2009**, *35*, 799−806.
(34) Geng, A. B.; Meng, L.; Han, J. Q.; Zhong, Q.; Li, M. R.; Han, S. G.; Mei, C. T.; Xu, L. J.; Tan, L.; Gan, L. Highly efficient visible-light photocatalyst based on cellulose derived carbon nanofiber/BiOBr composites. *Cellulose* **2018**, *25*, 4133−4144.
(35) Wang, Y. J.; Bai, X. J.; Pan, C. S.; He, J.; Zhu, Y. F. Enhancement of photocatalytic activity of Bi_2WO_6 hybridized with graphite-like C_3N_4. *J. Mater. Chem. A* **2012**, *22*, 11568−11573.
(36) Cui, L. P.; Shi, S.; Hou, W. S.; Yan, Z. F.; Dan, J. M. Hydrolysis and carbonization mechanism of cotton fibers in subcritical water. *New Carbon Mater.* **2018**, *33*, 245−251.
(37) Zhang, K.; Sun, P.; Khan, A.; Zhang, Y. Photochemistry of biochar during ageing process: Reactive oxygen species generation and benzoic acid degradation. *Sci. Total Environ.* **2021**, *765*, 144630.
(38) Huang, R. D.; Zhang, M. L.; Zheng, Z. Q.; Wang, K. Q.; Liu, X.; Chen, Q. Z.; Luo, D. X. Photocatalytic degradation of tobacco tar using $CsPbBr_3$ quantum dots modified Bi_2WO_6 composite photocatalyst. *Nanomaterials* **2021**, *11*, 2422.
(39) Djellabi, R.; Yang, B.; Xiao, K.; Gong, Y.; Cao, D.; Sharif, H. M. A.; Zhao, X.; Zhu, C.; Zhang, J. Unravelling the Mechanistic Role of Ti-O-C Bonding Bridge at Titania/Lignocellulosic Biomass Interface for Cr(VI) Photoreduction Under Visible Light. *J. Colloid Interface Sci.* **2019**, *553*, 409−417.
(40) Gholami, P.; Khataee, A.; Soltani, R.; Dinpazhoh, L.; Bhatnagar, A. Photocatalytic degradation of gemifloxacin antibiotic using Zn-Co-LDH@biochar nanocomposite. *J. Hazard. Mater.* **2020**, *382*, 121070.
(41) Wang, T. Y.; Zhong, S.; Zou, S.; Jiang, F. H.; Feng, L.; Su, X. Novel Bi_2WO_6-coupled Fe_3O_4 Magnetic Photocatalysts: Preparation, Characterization and Photodegradation of Tetracycline Hydrochloride. *Photochem. Photobiol.* **2017**, *93*, 1034−1042.
(42) Wang, T. Y.; Liu, S. X.; Mao, W.; Bai, Y. C.; Chiang, K.; Shah, K.; Paz-Ferreiro, J. Novel Bi_2WO_6 loaded N-biochar composites with enhanced photocatalytic degradation of rhodamine B and Cr(VI). *J. Hazard. Mater.* **2020**, *389*, 121827.

https://doi.org/10.1021/acsomega.3c01591
ACS Omega 2023, 8, 26882−26894

(43) Zhang, C.; Zhu, Y. Synthesis of Square Bi_2WO_6 Nanoplates as High-Activity Visible-Light-Driven Photocatalysts. *Chem. Mater.* **2005**, *17*, 3537−3545.
(44) Khachatryan, L.; Vejerano, E.; Lomnicki, S.; Dellinger, B. Environmentally Persistent Free Radicals (EPFRs). 1. Generation of Reactive Oxygen Species in Aqueous Solutions. *Environ. Sci. Technol.* **2011**, *45*, 8559−8566.
(45) Zhang, S.; Khan, I.; Qin, X.; Qi, K.; Liu, Y.; Bai, S. Construction of 1D Ag-AgBr/AlOOH Plasmonic Photocatalyst for Degradation of Tetracycline Hydrochloride. *Front. Chem.* **2020**, *8*, 117.
(46) Lwin, H. M.; Zhan, W.; Jia, F.; Song, S. Microwave-assisted hydrothermal synthesis of MoS_2-Ag_3PO_4 nanocomposites as visible light photocatalyst for the degradation of tetracycline hydrochloride. *Environ. Technol.* **2022**, *43*, 149−162.
(47) Tang, M.; Xia, Y. W.; Yang, D. X.; Lu, S. J.; Zhu, X. D.; Tang, R. Y.; Zhang, W. M. Ag Decoration and SnO_2 Coupling Modified Anatase/Rutile Mixed Crystal TiO_2 Composite Photocatalyst for Enhancement of Photocatalytic Degradation towards Tetracycline Hydrochloride. *Nanomaterials* **2022**, *12*, 873.
(48) Chung, H. Y.; Toe, C. Y.; Chen, W.; Wen, X.; Wong, R. J.; Amal, R.; Abdi, F. F.; Ng, Y. H. Manipulating the Fate of Charge Carriers with Tungsten Concentration: Enhancing Photoelectrochemical Water Oxidation of Bi_2WO_6. *Small* **2021**, *17*, 2102023.
(49) Li, K. X.; Huang, Z. A.; Zhu, S. Y.; Luo, S. L.; Yan, L. S.; Dai, Y. H.; Guo, Y. H.; Yang, Y. X. Removal of Cr(VI) from water by a biochar-coupled g-C_3N_4 nanosheets composite and performance of a recycled photocatalyst in single and combined pollution systems. *Appl. Catal., B* **2019**, *243*, 386−396.
(50) Wang, J.; Zhang, Q.; Deng, F.; Luo, X. B.; Dionysiou, D. D. Rapid toxicity elimination of organic pollutants by the photocatalysis of environment-friendly and magnetically recoverable step-scheme $SnFe_2O_4$/$ZnFe_2O_4$ nano-heterojunctions. *Chem. Eng. J.* **2020**, *379*, 122264.
(51) Xie, Q.; He, W. M.; Liu, S. W.; Li, C. H.; Zhang, J. F.; Wong, P. K. Bifunctional S-scheme g-C_3N_4/Bi/$BiVO_4$ hybrid photocatalysts toward artificial carbon cycling. *Chin. J. Catal.* **2020**, *41*, 140−153.
(52) Xu, T.; Zhang, L.; Cheng, H.; Zhu, Y. Significantly Enhanced Photocatalytic Performance of ZnO via Graphene Hybridization and the Mechanism Study. *Appl. Catal., B* **2011**, *101*, 382−387.
(53) Liang, Q.; Zhang, M.; Liu, C.; Xu, S.; Li, Z. Sulfur-doped graphitic carbon nitride decorated with zinc phthalocyanines towards highly stable and efficient photocatalysis. *Appl. Catal., A* **2016**, *519*, 107−115.
(54) Wang, S.; Chen, D.; Niu, F.; Zhang, N.; Qin, L.; Huang, Y. Pd cocatalyst on Sm-doped $BiFeO_3$ nanoparticles: synergetic effect of a Pd cocatalyst and samarium doping on photocatalysis. *RSC Adv.* **2016**, *6*, 34574−34587.
(55) Darr, J. A.; Zhang, J.; Makwana, N. M.; Weng, X. Continuous Hydrothermal Synthesis of Inorganic Nanoparticles: Applications and Future Directions. *Chem. Rev.* **2017**, *117*, 11125−11238.
(56) Wight, A. P.; Davis, M. E. Design and Preparation of Organic−Inorganic Hybrid Catalysts. *Chem. Rev.* **2002**, *102*, 3589−3614.
(57) Wu, F.; Liu, W.; Qiu, J.; Li, J.; Zhou, W.; Fang, Y.; Zhang, S.; Li, X. Enhanced photocatalytic degradation and adsorption of methylene blue via TiO_2 nanocrystals supported on graphene-like bamboo charcoal. *Appl. Surf. Sci.* **2015**, *358*, 425−435.
(58) Zhai, Y.; Dai, Y.; Guo, J.; Zhou, L.; Chen, M.; Yang, H.; Peng, L. Novel biochar@$CoFe_2O_4$/Ag_3PO_4 photocatalysts for highly efficient degradation of bisphenol a under visible-light irradiation. *J. Colloid Interface Sci.* **2020**, *560*, 111−121.
(59) Di, J.; Xia, J. X.; Ge, Y. P.; Li, H. P.; Ji, H. Y.; Xu, H.; Zhang, Q.; Li, H. M.; Li, M. N. Novel visible-light-driven CQDs/Bi_2WO_6 hybrid materials with enhanced photocatalytic activity toward organic pollutants degradation and mechanism insight. *Appl. Catal., B* **2015**, *168−169*, 51−61.
(60) Zhang, S.; Yin, Z.; Xie, L.; Yi, J.; Tang, W.; Tang, T.; Chen, J.; Cao, S. Facet engineered TiO_2 hollow sphere for the visible-light-mediated degradation of antibiotics via ligand-to-metal charge transfer. *Ceram. Int.* **2020**, *46*, 8949−8957.
(61) Tang, Y. D.; Li, T.; Xiao, W. X.; Huang, Z. T.; Wen, H. C.; Situ, W. B.; Song, X. L. Degradation mechanism and pathway of tetracycline in milk by heterojunction N-TiO_2-Bi_2WO_6 film under visible light. *Food Chem.* **2023**, *401*, 134082.
(62) Kumar, A.; Kumar, S.; Bahuguna, A.; Kumar, A.; Sharma, V.; Krishnan, V. Recyclable, bifunctional composites of perovskite type N-$CaTiO_3$ and reduced graphene oxide as an efficient adsorptive photocatalyst for environmental remediation. *Mater. Chem. Front.* **2017**, *1*, 2391−2404.
(63) Rohani Bastami, T.; Ahmadpour, A.; Ahmadi Hekmatikar, F. Synthesis of Fe_3O_4/Bi_2WO_6 nanohybrid for the photocatalytic degradation of pharmaceutical ibuprofen under solar light. *J. Ind. Eng. Chem.* **2017**, *51*, 244−254.
(64) Sheng, J. Y.; Li, X. J.; Xu, Y. M. Generation of H_2O_2 and OH Radicals on Bi_2WO_6 for Phenol Degradation under Visible Light. *ACS Catal.* **2014**, *4*, 732−737.

https://doi.org/10.1021/acsomega.3c01591
ACS Omega 2023, 8, 26882−26894